

MRAM-based Analog Sigmoid Function for In-memory Computing

Md Hasibul Amin, Mohammed Elbity, Mohammadreza Mohammadi, Ramtin Zand
Department of Computer Science and Engineering, University of South Carolina, Columbia, SC, 29201, USA

ABSTRACT

We propose an analog implementation of the transcendental activation function leveraging two spin-orbit torque magnetoresistive random-access memory (SOT-MRAM) devices and a CMOS inverter. The proposed analog neuron circuit consumes $1.8 - 27\times$ less power, and occupies $2.5 - 4931\times$ smaller area, compared to the state-of-the-art analog and digital implementations. Moreover, the developed neuron can be readily integrated with memristive crossbars without requiring any intermediate signal conversion units. The architecture-level analyses show that a fully-analog in-memory computing (IMC) circuit that use our SOT-MRAM neuron along with an SOT-MRAM based crossbar can achieve more than $1.1\times$, $12\times$, and $13.3\times$ reduction in power, latency, and energy, respectively, compared to a mixed-signal implementation with analog memristive crossbars and digital neurons. Finally, through cross-layer analyses, we provide a guide on how varying the device-level parameters in our neuron can affect the accuracy of multilayer perceptron (MLP) for MNIST classification.

1 INTRODUCTION

In-memory computing (IMC) systems, as an alternative for von Neuman architectures, aim to eliminate the expensive data movement between processor and memory in data-intensive applications such as machine learning (ML) by implementing computation where the data exist. IMC architectures leverage massive parallelism in memristive crossbars and analog computation to aggressively reduce the computational time complexity of matrix-vector multiplication (MVM) operations in ML workloads. However, there are still a wide range of computational tasks in ML workloads that cannot be performed in crossbars, e.g., activation functions and subsampling layers. The solution offered in most of the existing IMC architectures such as ISAAC [1], PUMA[2], and PRIME [3], is to design digital circuits for some of these functions, and place them near crossbars. Although this approach reduces the off-chip data transfer overhead between processor and memory for commonly-used functions, it requires analog-to-digital converter (ADC) and digital-to-analog converter (DAC) units to transfer the data between crossbars and digital functional units. According to a research by HP Labs [4], the signal converters and peripheral circuitry in IMC circuits can contribute to up to 90% and 95% of the total power consumption and area occupation, respectively. Therefore, reducing the need for signal conversion units in an IMC architecture can potentially lead to significant energy improvements.

Transcendental activation functions such as sigmoid and hyperbolic tangent (tanh) provide the desired nonlinear behavior which can be useful for a variety of ML models such as multilayer perceptron (MLP) and Long Short-Term Memory (LSTM). However, due to their hardware implementation challenges, alternative nonlinear

activation functions such as rectified linear unit (ReLU), first proposed in [5], have become popular in modern deep learning models such as convolutional neural networks (CNNs) [6, 7]. Hardware implementation of sigmoid and tanh functions have been widely investigated in the digital domain.

Direct implementations based on high-order polynomials, Taylor's series, and Maclaurin series offer high precision at the expense of high power consumption [8]. On the other hand, CORDIC-based hardware implementation [9] can achieve high accuracy and reduced area, however they have a high latency. In the PWL technique the non-linear function is separated into several linear segments to reduce implementation complexity [10]. Higher precision can be accomplished by increasing the number of linear segments at the cost of more hardware resource utilization. Among the several function approximation approaches, LUT methods are the fastest [11], but it requires large amount of memory to provide high accuracy.

Although digital hardware can provide an exact implementation of the ideal sigmoid function and is more robust to noise, its high power, area, and latency overheads have motivated the research on analog transcendental activation functions. In [12], three NMOS and three PMOS transistors are carefully sized to approximate a sigmoid activation function with only one reference voltage to bias the transistors. In [13], an NMOS and a PMOS transistors with large width/length ratios are utilized along with a resistor load to realize *tanh*-like activation function. While, both of these design achieve significant reductions in power and area compared to digital implementations, they still require large transistors. In this paper, we leverage spin-orbit torque magnetoresistive random-access memory (SOT-MRAM) devices and a simple CMOS inverter to develop a sigmoid activation function that is compatible with memristive crossbars. We exhibit the direct and indirect energy and performance benefits of our proposed analog neuron for the IMC architectures through the circuit implementation of a fully-analog MLP circuit and comparing it with existing mixed-signal designs. While MRAM technology has been previously used for realizing probabilistic sigmoidal activation functions in binary stochastic neurons [14, 15], this is the first work which leverages MRAM devices to implement a transcendental activation function.

2 SOT-MRAM TECHNOLOGY

MRAM device is one of the promising memristive technologies that have been widely investigate for the IMC circuits and architectures [15, 16]. The magnetic tunnel junctions (MTJs) are the main building block in MRAM devices. MTJs include two ferro-magnetic (FM) layers that are separated by a thin oxide layer as shown in Figure 1. The magnetization direction of electrons in one of the FM layers (reference layer) is fixed, whereas the direction of electrons in the other FM layer (free layer) can be switched. The resistance levels of MTJ are determined by the angle (θ) between the magnetization

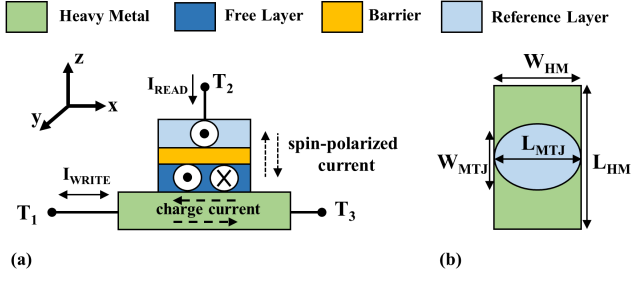


Figure 1: (a) SOT-MRAM cell. A charge current along $+x/-x$ generates a spin-polarized current in $+z$ direction producing a spin torque that switches the magnetic direction of the free layer in $+y/-y$ direction. (b) SOT-MRAM Top view.

Table 1: Parameters of the SOT-MRAM device [18]

Parameter	Description	Value
MTJ_{Area}	$l_{MTJ} \times w_{MTJ} \times \frac{\pi}{4}$	$50nm \times 30nm \times \frac{\pi}{4}$
HM_V	$l_{HM} \times w_{HM} \times t_{HM}$	$100nm \times 50nm \times 3nm$
ρ_{HM}	heavy metal resistivity	$200\mu\Omega.cm$
RA	resistance-area product	$10 \Omega.\mu m^2$
V_0	Fitting parameter	0.65
TMR_0	tunneling magnetoresistance	100

orientation of the FM layers. The following equations can be used to calculate the resistance of the MTJ in parallel (P) and antiparallel (AP) magnetization configurations [17, 18]:

$$R(\theta) = \frac{2R_{MTJ}(1 + TMR)}{2 + TMR(1 + \cos \theta)} = \begin{cases} R_P = R_{MTJ}, & \theta = 0 \\ R_{AP} = R_{MTJ}(1 + TMR), & \theta = \pi \end{cases} \quad (1)$$

$$TMR(T, V_b) = \frac{TMR_0/100}{1 + (\frac{V_b}{V_0})^2} \quad (2)$$

where $R_{MTJ} = \frac{RA}{Area}$. The MTJ's resistance-area product (RA) value is determined by the material composition of its layers. TMR stands for tunneling magnetoresistance, and it is determined by temperature (T) and bias voltage (V_b). TMR_0 is a material-dependent constant, and V_0 is a fitting parameter.

SOT-MRAM device [19] is a class of MRAM technology, in which the magnetization direction of the free layer can be changed by means of a spin-polarized current produced by a charge current passing through a heavy metal (HM), as shown in Fig. 1. The resistance of the HM can be calculated using the below equation:

$$R_{HM} = \rho_{HM} \cdot l_{HM} / w_{HM} \cdot t_{HM} \quad (3)$$

where ρ_{HM} , l_{HM} , w_{HM} , t_{HM} are the resistivity, length, width, and thickness of the HM, respectively. Here, we use the aforementioned MTJ and HM equations to create a Verilog-A model of the SOT-MRAM device for circuit simulations using the parameters mentioned in Table 1 as default values.

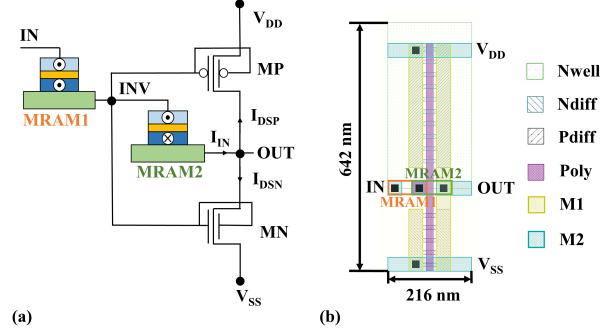


Figure 2: (a) Schematic of the proposed analog sigmoid neuron (b) Layout design.

3 MRAM-BASED SIGMOID NEURON

Our proposed SOT-MRAM-based sigmoid neuron incorporates two SOT-MRAM devices (MRAM1 and MRAM2) and a CMOS-based inverter, as shown in Figure 2. The SOT-MRAM devices are configured in opposite states where MRAM1 is in parallel state (R_P) and MRAM2 is in anti-parallel state (R_{AP}). The SOT-MRAM devices form a voltage divider which reduces the slope of the inverter's linear region leading to a smooth transition from V_{DD} to V_{SS} in the output node (OUT), when the input voltage node (IN) is swept from V_{SS} to V_{DD} . Herein, to verify that such circuit can realize a transcendental activation function between the input voltage (V_{IN}) and output voltage (V_{OUT}), we conducted a detailed circuit analysis as described in the followings.

First, we apply the Kirchhoff's current law at OUT node resulting in the following relation:

$$I_{IN} = I_{DSP} + I_{DSN} \quad (4)$$

where I_{IN} is the current from node IN to node OUT which passes through the MRAM devices (Fig. 2 (a)), and I_{DSP} and I_{DSN} are the drain-to-source currents for the PFET (or PMOS) device MP and NFET (or NMOS) device MN, respectively. Considering that no current flows towards the gates of the FinFETs, the I_{IN} can be calculated as follows based on the Ohm's law:

$$I_{IN} = \frac{V_{IN} - V_{OUT}}{R_P + R_{AP}} \quad (5)$$

where R_P and R_{AP} can be obtained from equations (1) and (2). Replacing I_{IN} in (4) with (5), we can calculate V_{OUT} as:

$$V_{OUT} = V_{IN} - [(R_P + R_{AP})(I_{DSP} + I_{DSN})] \quad (6)$$

The different regions of operation for our neuron can be identified based on the different operating regions of the MN and MP transistors. To find the operating region of the transistors, we need to calculate their gates' voltage, i.e., V_{INV} in Figure 2 (a). Since no current flows towards the gate of the transistors, V_{INV} can be calculated using the below equation:

$$V_{INV} = V_{IN} - \frac{V_{IN} - V_{OUT}}{R_P + R_{AP}} \times R_P \quad (7)$$

Table 2: Drain-to-source currents for different operating regions of MP and MN.

	Cut-off	Triode	Saturation
I_{DSP}	0	$\beta_P[(V_{INV} - V_{DD} - V_{TP})(V_{OUT} - V_{DD}) - \frac{(V_{OUT} - V_{DD})^2}{2}]$	$-\frac{\beta_P}{2}(V_{INV} - V_{DD} - V_{TP})^2$
I_{DSN}	0	$\beta_N[(V_{INV} - V_{SS} - V_{TN})(V_{OUT} - V_{SS}) - \frac{(V_{OUT} - V_{SS})^2}{2}]$	$-\frac{\beta_N}{2}(V_{INV} - V_{SS} - V_{TN})^2$

Table 3: Conditions for different operating regions of MP and MN with V_{TP} and V_{TN} threshold voltages, respectively.

	Cut-off	Triode	Saturation
MP	$V_{INV} > V_{DD} + V_{TP}$	$V_{INV} < V_{DD} + V_{TP}$ $V_{OUT} > V_{INV} - V_{TP}$	$V_{INV} < V_{DD} + V_{TP}$ $V_{OUT} < V_{INV} - V_{TP}$
MN	$V_{INV} < V_{SS} + V_{TN}$	$V_{INV} > V_{SS} + V_{TN}$ $V_{OUT} < V_{INV} - V_{TN}$	$V_{INV} > V_{SS} + V_{TN}$ $V_{OUT} > V_{INV} - V_{TN}$

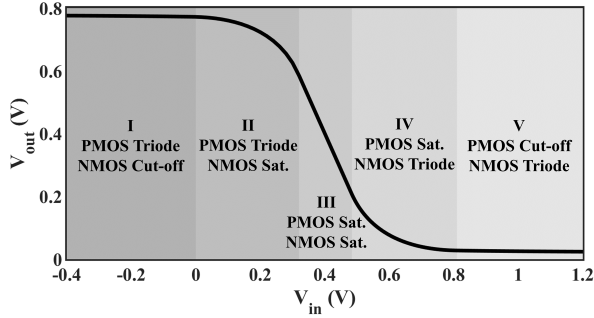


Figure 3: VTC of the proposed sigmoid neuron.

By using equation (7) and the relations listed in Table 3, we can find the operating region of the transistors, and consequently the operating regions of the proposed neuron, based on the input voltage V_{IN} . Once the regions are identified, we can use equation (6) and the I_{DSP} and I_{DSN} relations listed in Table 2 to find the relation between V_{OUT} and V_{IN} . Here, we utilized the MATLAB solver to obtain the relation between the output and input of the neuron. Based on the results, the neuron has five operating regions, the V_{OUT} for each of which is provided in Appendix A for better readability. To exhibit the relation between V_{OUT} and V_{IN} , we plotted the voltage transfer curve (VTC) of the neuron based on the equations obtained from the solver (refer to Appendix A) for $V_{DD}=0.8V$ and $V_{SS}=0$ as the nominal voltages for the 14nm High-Performance PTM-MG FinFET model [20] with $V_{TP}=-0.2V$ and $V_{TN}=0.2V$ threshold voltages. Figure 3 shows the neuron's VTC curve including the five operating regions. As shown, the proposed neuron can provide a transcendental-like activation function that can approximate a $V_{OUT} = \text{sigmoid}(-V_{IN})$ function. An actual $V_{OUT} = \text{sigmoid}(V_{IN})$ function can also be provided by inverting the V_{IN} before applying it to the proposed neuron. However, as it is described in the next section, inverting the input would not be necessary if the neural network is trained with the inverse sigmoid function.

4 RESULTS AND DISCUSSION

To investigate the features and benefits of the proposed neuron, we perform a hierarchical simulation process including device-, circuit-, and architecture-level analyses as described in the followings.

4.1 Device-level Analysis

To explore the impacts of device-level parameters such as TMR and RA on the shape of the sigmoid function, we implement the proposed neuron in SPICE circuit simulator using the Verilog-A model developed for the SOT-MRAM devices along with 14nm FinFET transistor model. Figure 4 shows how changing RA and TMR values in the SOT-MRAM can change the sigmoid function.

To analyze the effect of RA on our neuron, we vary the value of RA to 5, 10, 15 and 20 $\Omega\mu m^2$, while fixing the TMR to 200 (Fig. 4 (a)). For analyzing the effect of TMR, we keep the value of RA fixed to 15 $\Omega\mu m^2$ and sweep the value of TMR to 100, 200, 300 and 400, and plot the results in Figure 4 (b). The results show that changing TMR imposes larger variations in the shape of the function. However, to investigate how the shape of the sigmoid function can impact the entire network's accuracy, we trained a binarized $400 \times 120 \times 84 \times 10$ MLP model to classify MNIST [21] handwritten images with 20×20 pixels. We used $\text{sigmoid}(-x)$ activation function during the training to be compatible with the proposed neuron's sigmoidal shape. First, the model is trained for 20 epochs achieving an accuracy of roughly 97%. Next, the trained weights are mapped to an SOT-MRAM based crossbar. Finally, the proposed SOT-MRAM neuron is integrated with the crossbar and the corresponding IMC circuit is simulated by SPICE. Here, we do not explain the crossbar circuit implementation since it has been already well-investigated in the literature [4, 22]. Figure 5 (a) shows how the changes made to the shape of the sigmoid activation function caused by varying the TMR and RA values can impact the overall accuracy of the implemented IMC circuit. The results show that higher RA values consistently lead to better accuracy. However for TMR, the accuracy increases when changing its value from 100 to 200 but it significantly drops when TMR value is increased to 300 and 400. Thus, a maximum accuracy of 95.83% is achieved with TMR=200 and RA=20 $\Omega\mu m^2$, which is roughly 1% less than what was realized by ideal software implementation. The change in TMR and RA values can also affect the power consumption of the neuron

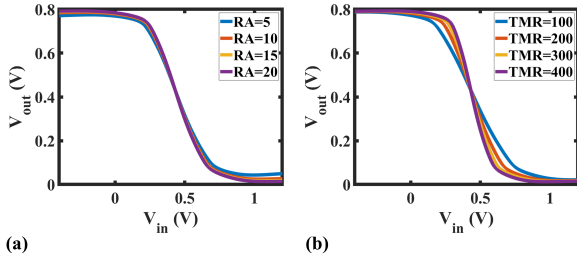


Figure 4: Effect of varying (a) RA (TMR is fixed to 200) and (b) TMR (RA is fixed to $15 \Omega\mu m^2$) on the reverse sigmoid output

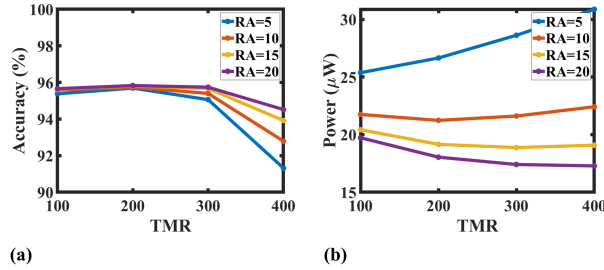


Figure 5: (a) MLP classification accuracy, and (b) neuron's power consumption for different values of TMR and RA.

as shown in Fig. 5 (b), according to which, higher RA and higher TMR values can lead to reduced power consumption.

4.2 Circuit-level Analysis

To compare our SOT-MRAM based sigmoid neuron with previous efficient digital [23, 10] and analog [12, 13] implementation of transcendental neurons, we conduct SPICE circuit simulations using 14nm technology node [24] and verilog-A model of the SOT-MRAM. For the area comparison, we designed the layout of our neuron as shown in figure 2 (b), which demonstrates an area occupation of $0.138 \mu m^2$. However, as the area occupation values of the previous neurons were measured based on older technology nodes, we use the scaling factors from [25] to scale-down their area to 14nm node to provide a fair comparison. For the power consumption comparison, we implemented the previous analog neurons [12, 13] and our SOT-MRAM neuron with 14nm technology node. For our neuron, we swept the input voltage from -2V to 2V and measure the average power consumption. However, the previous analog neurons [12, 13] take current as input unlike our proposed sigmoid neuron. For fair calculation of the average power consumption, we only consider the active range of their activation function, which we found to be from $-200\mu A$ to $200\mu A$. For the digital neurons, we scaled down their power consumption to 14nm technology using the scaling factors provided in [25]. The comparison results are listed in Table 4, according to which our neuron achieves roughly $27\times$ and $1.8\times$ power consumption and $4931\times$ and $2.5\times$ area reduction compared to the most power- and area-efficient digital and analog neurons, respectively.

Table 4: Comparison between the SOT-MRAM based neuron and previous digital and analog implementations.

	[23]	[10]	[12]	[13]	This work
Domain	Digital	Digital	Analog	Analog	Analog
Power (μW)	6.72×10^5	493.4	74.21	32.16	18.04
Area (μm^2)	9.3095	680.5	0.4975	0.3505	0.138

Table 5: Power consumption and latency breakdowns of the fully-analog and mixed-signal implementations of MLP.

		Mixed-Signal		Fully-Analog	
		Power (mW)	Latency (Clocks)	Power (mW)	Latency (Clocks)
Layer 1	DAC	3.463		3.463	
	Crossbar	221.965			
	Neuron	59.208	4		
	ADC	5.037			
Layer 2	DAC	1.039		238.405	
	Crossbar	12.225			
	Neuron	41.446	4		
	ADC	3.526			
Layer 3	DAC	0.727		0.42	
	Crossbar	1.204			
	Neuron	4.934	4		
	ADC	0.42			

Table 6: Total energy, power, and latency comparison between fully-analog and mixed signal MLP implementations

	Power(W)	Latency(ns)	Energy(nJ)	TOPS/W
Mixed-Signal	0.355	48	17.04	3.41
Fully-Analog	0.242	4	0.968	60.86

4.3 Architecture-level Analysis

To investigate the benefits of the proposed analog sigmoid at the architecture level, we develop a fully-analog IMC architecture that integrates our SOT-MRAM neuron with an analog memristive crossbar to realize the MVM operations and activations functions in a single fully-connected layer. These analog circuits can be readily integrated to form MLP architectures without requiring intermediate signal conversion units. The only signal converters needed for the fully-analog IMC architecture is a DAC unit in the first layer to convert the digital inputs from a CPU to analog signals, and one ADC unit to convert the analog output of the IMC to digital values to be transferred to the CPU. We compare our design with a conventional mixed-signal IMC architectures which use analog crossbars along with digital neurons, thus imposing the need for DAC and ADC units in every layer. The schematic of both of these designs for implementing the $400 \times 120 \times 84 \times 10$ MLP model discussed in section 4.1 is shown in Figure 6, in which the number of neurons, DACs, ADCs and the size of the crossbars in each layer is identified separately.

Table 5 shows the breakdown of the power consumption and latency in the fully-analog IMC and mixed-signal IMC. Here, we utilized a low-power successive-approximation (SAR) ADC and a capacitive DAC proposed in [26] for signal conversion. We scaled-down their power consumption from the original 65nm technology

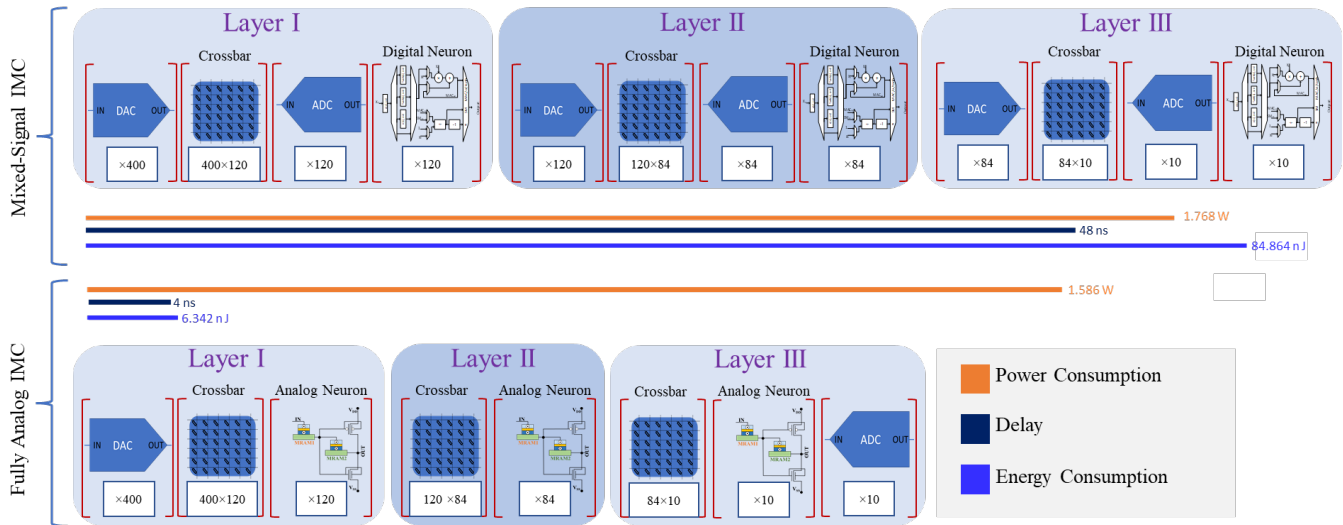


Figure 6: The schematic of the mixed-signal and the fully-analog IMC implementations for a $400 \times 120 \times 84 \times 10$ MLP.

to 14nm technology which gives us $41.98\mu W$ and $8.66\mu W$ power consumption for a single ADC and DAC block, respectively. For the mixed-signal implementation, we used the more efficient digital neuron design [13], which requires three clocks with 250MHz frequency to execute the activation function. Other than the neuron the entire DAC, crossbar, and ADC operations can be completed in one clock cycle. Thus, in the mixed-signal MLP implementation, each layer requires four clock cycles, while the entire fully-analog MLP implementation can be executed in one clock cycles. As for the power consumption, the fully-analog implementation saves power through the elimination of the intermediate conversion units, connecting all crossbars, and the use of power-efficient analog neurons, which are all achieved by using the SOT-MRAM based sigmoid neuron proposed herein. The total power, latency, energy, and performance in terms of tera operations per second per Watt (TOPS/W) of fully-analog and mixed-signal IMC architectures are listed in table 6. The results obtained show approximately 13× improvement in terms of the TOPS/W.

5 CONCLUSION

We proposed a power- and area-efficient SOT-MRAM based neuron circuit realizing an analog sigmoid activation function. Through a hierarchical simulation process, we show the characteristics and benefits of our proposed neuron across device, circuit, and architecture levels. Besides the direct performance and power benefits that can be achieved by the proposed neuron compared to the state-of-the-art, it is shown that it can be readily integrated with analog memristive crossbars without requiring any signal conversion that obviates the need for power-hungry DAC and ADC units. Simulation results exhibited that a fully-analog IMC architecture using our proposed neuron achieves more than 13× improvement in TOPS/W compared to the mixed-signal IMC implementations that utilize analog crossbars along with digital neurons.

REFERENCES

- [1] Ali Shafiee, Anirban Nag, Naveen Muralimanohar, Rajeev Balasubramonian, John Paul Strachan, Miao Hu, R. Stanley Williams, and Vivek Srikumar. 2016. Isaac: a convolutional neural network accelerator with in-situ analog arithmetic in crossbars. In (ISCA '16). IEEE Press, Seoul, Republic of Korea, 14–26.
- [2] Aayush Ankit, Izzat El Hajj, Sai Rahul Chalamalasetti, Geoffrey Ndu, Martin Foltin, R. Stanley Williams, Paolo Faraboschi, Wen-mei W Hwu, John Paul Strachan, Kaushik Roy, and Dejan S. Milojicic. 2019. Puma: a programmable ultra-efficient memristor-based accelerator for machine learning inference. In *Proceedings of the Twenty-Fourth International Conference on Architectural Support for Programming Languages and Operating Systems (ASPLOS '19)*. Association for Computing Machinery, Providence, RI, USA, 715–731.
- [3] Ping Chi, Shuangchen Li, Cong Xu, Tao Zhang, Jishen Zhao, Yongpan Liu, Yu Wang, and Yuan Xie. 2016. Prime: a novel processing-in-memory architecture for neural network computation in eram-based main memory. *ACM SIGARCH Computer Architecture News*, 44, 3, 27–39.
- [4] Miao Hu, John Paul Strachan, Zhiyong Li, Emmanuelle M. Grafals, Noraica Davila, Catherine Graves, Sity Lam, Ning Ge, Jianhua Joshua Yang, and R. Stanley Williams. 2016. Dot-product engine for neuromorphic computing: programming 111m crossbar to accelerate matrix-vector multiplication. In *2016 53rd ACM/EDAC/IEEE Design Automation Conference (DAC)*, 1–6.
- [5] Alex Krizhevsky, Ilya Sutskever, and Geoffrey E Hinton. 2012. Imagenet classification with deep convolutional neural networks. In *Advances in Neural Information Processing Systems 25*. F. Pereira, C. J. C. Burges, L. Bottou, and K. Q. Weinberger, editors. Curran Associates, Inc., 1097–1105.
- [6] Karen Simonyan and Andrew Zisserman. 2014. Very deep convolutional networks for large-scale image recognition. *arXiv preprint arXiv:1409.1556*.
- [7] Christian Szegedy, Wei Liu, Yangqing Jia, Pierre Sermanet, Scott Reed, Dragomir Anguelov, Dumitru Erhan, Vincent Vanhoucke, and Andrew Rabinovich. 2015. Going deeper with convolutions. In *Proceedings of the IEEE conference on computer vision and pattern recognition*, 1–9.
- [8] B. Lee and N. Burgess. 2003. Some results on taylor-series function approximation on fpga. In *The Thirty-Seventh Asilomar Conference on Signals, Systems Computers, 2003*. Volume 2, 2198–2202 Vol.2.
- [9] Hui Chen, Lin Jiang, Yuanyong Luo, Zhonghai Lu, Yuxiang Fu, Li Li, and Zongguang Yu. 2020. A cordic-based architecture with adjustable precision and flexible scalability to implement sigmoid and tanh functions. In *2020 IEEE International Symposium on Circuits and Systems (ISCAS)*, 1–5.
- [10] Guido Baccelli, Dimitrios Stathis, Ahmed Hemani, and Maurizio Martina. 2020. Nacu: a non-linear arithmetic unit for neural networks. In *2020 57th ACM/IEEE Design Automation Conference (DAC)*, 1–6.
- [11] Pramod Kumar Meher. 2010. An optimized lookup-table for the evaluation of sigmoid function for artificial neural networks. In *2010 18th IEEE/IFIP International Conference on VLSI and System-on-Chip*, 91–95.
- [12] G. Khodabandehloo, M. Mirhassani, and M. Ahmadi. 2012. Analog implementation of a novel resistive-type sigmoidal neuron. *IEEE Trans. Very Large Scale Integr. (VLSI) Syst.*, 20, 4, 750–754.

- [13] J. Shamsi, A. Amirsoleimani, S. Mirzakuchaki, A. Ahmade, S. Alirezaee, and M. Ahmadi. 2015. Hyperbolic tangent passive resistive-type neuron. In *IEEE International Symposium on Circuits and Systems (ISCAS)*.
- [14] Ramtin Zand, Kerem Y Camsari, Supriyo Datta, and Ronald F DeMara. 2018. Composable probabilistic inference networks using mram-based stochastic neurons. *arXiv preprint arXiv:1811.11390*.
- [15] Ramtin Zand, Kerem Yunus Camsari, Steven D. Pyle, Ibrahim Ahmed, Chris H. Kim, and Ronald F. DeMara. 2018. Low-energy deep belief networks using intrinsic sigmoidal spintronic-based probabilistic neurons. In *Proceedings of the 2018 on Great Lakes Symposium on VLSI (GLSVLSI '18)*. Chicago, IL, USA, 15–20.
- [16] Mohammed Elbtity, Abhishek Singh, Brendan Reidy, Xiaochen Guo, and Ramtin Zand. 2021. An in-memory analog computing co-processor for energy-efficient cnn inference on mobile devices. *2021 IEEE Computer Society Annual Symposium on VLSI (ISVLSI)*, 2021.
- [17] Y. Zhang, W. Zhao, Y. Lakys, J. O. Klein, J. V. Kim, D. Ravelosona, and C. Chappert. 2012. Compact modeling of perpendicular-anisotropy cofeb/mgo magnetic tunnel junctions. *IEEE Transactions on Electron Devices*, 59, 3, 819–826.
- [18] Ramtin Zand, Arman Roohi, and Ronald F DeMara. 2018. Fundamentals, modeling, and application of magnetic tunnel junctions. *Nanoscale Devices: Physics, Modeling, and Their Application*, 337.
- [19] L. Liu, C.F. Pai, Y. Li, H. W. Tseng, D. C. Ralph, and R. A. Buhrman. 2012. Spin-torque switching with the giant spin hall effect of tantalum. *Science*, 336, 6081, 555–558.
- [20] 2012. Predictive technology model. <http://ptm.asu.edu>. (2012).
- [21] Y. Lecun, L. Bottou, Y. Bengio, and P. Haffner. 1998. Gradient-based learning applied to document recognition. *Proceedings of the IEEE*, 86, 11, 2278–2324.
- [22] Md Hasibul Amin, Mohammed Elbtity, and Ramtin Zand. 2022. Interconnect parasitics and partitioning in fully-analog in-memory computing architectures. In *2022 IEEE International Symposium on Circuits and Systems (ISCAS)*.
- [23] Gunjan Rajput, Gopal Raut, Mahesh Chandra, and Santosh Kumar Vishvakarma. 2021. Vlsi implementation of transcendental function hyperbolic tangent for deep neural network accelerators. *Microprocessors and Microsystems*, 84, 104270.
- [24] Saurabh Sinha, Greg Yeric, Vikas Chandra, Brian Cline, and Yu Cao. 2012. Exploring sub-20nm finfet design with predictive technology models. In *DAC Design Automation Conference 2012*, 283–288.
- [25] Aaron Stillmaker and Bevan Baas. 2017. Scaling equations for the accurate prediction of CMOS device performance from 180 nm to 7 nm. *Integration*, 58, (June 2017), 74–81.
- [26] Jeevani Kommarreddy. 2019. 10-bit c2c dac design in 65nm cmos technology. In *Browse all Theses and Dissertations. 2112*. https://corescholar.libraries.wright.edu/etd_all/2112.

A SOLVING THE NEURON EQUATIONS

Equation 10-14 refers to the calculated analytical solutions for five different operating regions of the proposed sigmoid function, respectively. We define two more intermediate parameters T_1 and T_2 for better readability of the equations as follows:

$$T_1 = \beta_P^2 R_{AP}^2 (V_{DD} - V_{IN} + V_{TP})^2 + \beta_P^2 R_P^2 V_{TP}^2 + 2\beta_P^2 R_{AP} R_P V_{TP}^2 + 2\beta_P R_P (V_{DD} - V_{IN} + V_{TP}) + 2\beta_P R_{AP} V_{TP} + 1 \quad (8)$$

$$T_2 = \beta_N^2 R_{AP}^2 (V_{IN} - V_{TN})^2 + \beta_N^2 R_P^2 V_{TN}^2 + 2\beta_N^2 R_{AP} R_P V_{TN} (V_{TN} - V_{IN}) - 2\beta_N R_{AP} V_{TN} + 2\beta_N R_P (V_{IN} - V_{TN}) + 1 \quad (9)$$

Equation 10 refers to the output of the region I from figure 3 where MP and MN stay in the triode and cut-off region, respectively.

$$V_{OUT} = \frac{-1 - \beta_P R_P (V_{DD} + V_{TP}) + \beta_P R_{AP} (V_{IN} - V_{TP}) + T_1^{1/2}}{\beta_P (R_{AP} - R_P)} \quad (10)$$

In region II, MN switches to the saturation state and MP remains in the triode state. Equation 11 refers to the output for the region II.

$$V_{OUT} = [R_P - R_{AP} - \beta_P R_P^2 (V_{DD} - V_{TN} + V_{TP}) - \beta_P R_{AP}^2 (V_{IN} - V_{TP}) + \beta_P R_{AP} R_P (V_{DD} - V_{IN}) + \beta_N R_{AP} R_P (V_{IN} - V_{TN}) + (R_{AP} + R_P) \{T_1 - \beta_N \beta_P R_{AP}^2 (V_{IN} - V_{TN})^2 - \beta_N \beta_P R_P^2 ((V_{DD} - V_{TN})^2 + V_{TP} (V_{DD} - V_{TN})) + 2\beta_N R_P (V_{IN} - V_{TN})\}^{1/2}] / (\beta_P R_{AP}^2 - \beta_P R_P^2 + \beta_N R_P^2) \quad (11)$$

In the next region, MN and MP both work in the saturation region. Equation 12 refers to the output equation for the region III.

$$V_{OUT} = [R_P - R_{AP} - \beta_P R_P^2 (V_{DD} - V_{TN} + V_{TP}) - \beta_P R_{AP} R_P (V_{DD} - V_{IN}) - \beta_N R_{AP} R_P (V_{IN} - V_{TN}) + (R_{AP} + R_P) \{2\beta_P R_P (V_{DD} - V_{IN} + V_{TP}) - 2\beta_N R_P V_{TN} - \beta_N \beta_P R_P^2 ((V_{DD} - V_{TN})^2 + V_{TP} (V_{TP} - 2V_{TN} + 2V_{DD})) + 1\}^{1/2}] / (\beta_N R_P^2 - \beta_P R_P^2) \quad (12)$$

At region IV, MN switches to the triode region while MP stays in the saturation region. (13) refers to the output for this region:

$$V_{OUT} = [R_P + R_{AP} - \beta_P R_P^2 (V_{DD} + V_{TP}) + \beta_N R_P^2 V_{TN} - \beta_N R_{AP}^2 (V_{IN} - V_{TN}) + \beta_P R_{AP} R_P (V_{DD} - V_{IN} + V_{TP}) + \beta_N R_{AP} R_P (V_{IN} - 2V_{TN}) + (R_{AP} + R_P) \{T_2 - \beta_N \beta_P R_{AP}^2 (V_{DD}^2 + V_{TP}^2 - 2V_{DD} V_{IN} + V_{TP} (V_{DD} - V_{IN})) - \beta_N \beta_P R_P^2 ((V_{DD} + V_{TP})^2 - V_{TN} (V_{DD} + V_{TP})) + 2\beta_P R_P (V_{DD} - V_{IN} + V_{TP}) + 2\beta_P R_{AP} V_{TP}\}^{1/2}] / (\beta_P R_{AP}^2 - \beta_P R_P^2 + \beta_N R_P^2) \quad (13)$$

Finally, MP switches to the cut-off region while MN remains in the triode region. Equation 14 refers to the output of the region V.

$$V_{OUT} = \frac{1 + \beta_N R_{AP} (V_{IN} - V_{TN}) - \beta_N R_P V_{TN} - T_2^{1/2}}{\beta_N (R_{AP} - R_P)} \quad (14)$$